bioRxiv preprint doi: https://doi.org/10.1101/134999; this version posted May 6, 2017. The copyright holder for this preprint (which was not certified by peer review) is the author/funder. All rights reserved. No reuse allowed without permission.

A carbon nanotube optical reporter maps endolysosomal lipid flux

Prakrit V. Jena[†1], Daniel Roxbury[†5], Thomas V. Galassi[1,2], Leila Akkari[1,3], Christopher P. Horoszko[1,2], David B. Iaea[2], Januka Budhathoki-Uprety[1], Nina H. Pipalia[2], Abigail S. Haka[2], Jackson D. Harvey[1,2], Jeetain Mittal[4], Frederick R. Maxfield[2], Johanna A. Joyce[1,2,3], Daniel A. Heller[1,2*]

[1]Memorial Sloan Kettering Cancer Center, New York, NY 10065

[2]Weill Cornell Medical College, New York, NY 10065

[3]Ludwig Institute for Cancer Research, University of Lausanne, Switzerland, CH 1066

[4]Lehigh University, Bethlehem, PA 18015

[5]University of Rhode Island, Kingston, RI 02881

† Contributed equally to this work

* Corresponding author. Email: hellerd@mskcc.org

bioRxiv preprint doi: https://doi.org/10.1101/134999; this version posted May 6, 2017. The copyright holder for this preprint (which was not certified by peer review) is the author/funder. All rights reserved. No reuse allowed without permission.

Abstract:

Lipid accumulation within the lumen of endolysosomal vesicles is observed in various pathologies including atherosclerosis, liver disease, neurological disorders, lysosomal storage disorders, and cancer. Current methods cannot measure lipid flux specifically within the lysosomal lumen of live cells. We developed an optical reporter, composed of a photoluminescent carbon nanotube of a single chirality, which responds to lipid accumulation via modulation of the nanotube's optical bandgap. The reporter localizes exclusively to the lysosomal lumen where the emission wavelength can be spatially resolved to generate quantitative maps of lipid content. Measurements of patient-derived Niemann-Pick type C fibroblasts identified lipid accumulation and phenotypic reversal of this lysosomal storage disease. The reporter discerned sub-cellular differences in lipid content, illuminating significant intracellular heterogeneity among lysosomes of differentiating bone marrow-derived monocytes. Single-cell kinetics of lipoprotein-derived cholesterol accumulation within macrophages revealed rates that differed among cells by an order of magnitude. This carbon nanotube-based reporter confers new capabilities for drug development and the investigation of lipid-linked diseases.

Lysosomes are vacuolar organelles responsible for the breakdown of lipids, proteins, sugars, and other cellular materials[1]. The failure to catabolize or export lysosomal contents can result in lysosomal storage disorders (LSDs), a family of approximately 50 diseases characterized by the accumulation of undigested substrates, such as lipids and glycoproteins, within the lysosomal lumen due to an inherited defect in a single protein[2, 3]. Lipid accumulation in the lysosomal lumen is observed in many LSDs as well as during atherosclerotic foam cell formation[4], the

bioRxiv preprint doi: https://doi.org/10.1101/134999; this version posted May 6, 2017. The copyright holder for this preprint (which was not certified by peer review) is the author/funder. All rights reserved. No reuse allowed without permission.

transition from steatosis to non-alcoholic steatohepatitis[5], in multiple neurological disorders[6], cancer[7], and drug-induced phospholipidosis (DIPL)[8]. The search for small molecule therapeutics against lysosomal storage disorders is hampered by the limited number of tools available to assay lipid content exclusively within the lysosomes of live cells[9].

Although multiple classes of sensors and imaging modalities exist to study lipids, current probes are limited in their capabilities`. Stains such as LipidTox can detect the general accumulation of lipids within cells[10] but are not organelle-specific. Fluorophore-conjugated and intrinsically fluorescent lipid analogs are used for analyzing lipid trafficking[10]. Lipid analogs, synthesized by conjugation of a fluorophore to a modified lipid, allow the tracking of uptake and incorporation of lipids into the cell membrane[11, 12]. Lipid dynamics can be tracked in live cells using fluorescent proteins fused with lipid-binding domains, however the expressed domains can hamper the native function of the lipid[13]. Environmentally-sensitive fluorophores were recently developed which respond to lipid order[14] and can be tracked in cell membranes undergoing processes such as endosomal maturation[15]. The bulk of these technologies are useful for studying lipids present within a biological membrane, but, to the best of our knowledge, no existing probe specifically localizes to the lysosomal lumen or measures the lipid content specifically within the limiting membrane.

To develop a biocompatible fluorescent reporter for lipids in the endolysosomal lumen, we investigated the unique physicochemical properties of single-walled carbon nanotubes (SWCNTs). Semiconducting SWCNTs emit highly photostable and narrow-bandwidth near-infrared photoluminescence[16], which is sensitive to local perturbations[17]. The SWCNT emission energy responds to the solvent environment[18] by producing a solvatochromic energy shift[19]. This response has been used to detect conformational polymorphism[20] of DNA non-covalently

bioRxiv preprint doi: https://doi.org/10.1101/134999; this version posted May 6, 2017. The copyright holder for this preprint (which was not certified by peer review) is the author/funder. All rights reserved. No reuse allowed without permission.

complexed to a nanotube, as well as damage to DNA bases[21], via solvatochromic energy shifts down to ≤1 nm.

Here, we present a biocompatible carbon nanotube optical reporter of lipids within the endolysosomal lumen of live cells. Composed of a non-covalent complex consisting of an amphiphilic polymer and a single (n,m) species (chirality) of carbon nanotube, the reporter exhibits a solvatochromic shift of over 13 nm in response to biological lipids. In mammalian cells, the reporter remains within the endolysosomal pathway and localizes specifically to the lumen of late endosomes and lysosomes (LE/Ly). Using near-infrared hyperspectral microscopy, we spatially resolved the solvatochromic response of the reporter to lipids in the lysosomal lumen and obtained quantitative lipid maps of live cells with sub-cellular resolution. Emission from the reporter identified the lysosomal storage disease Niemann-Pick type C (NPC) in fibroblasts from an NPC patient. Furthermore, the reporter benchmarked treatment, exhibiting a distinct signal reversal upon administration of hydroxypropyl-β-cyclodextrin, a drug that reverses the disease phenotype. Additionally, lysosomal lipid accumulation was detected using spectroscopy alone, in a 96-well plate format compatible with high-throughput drug screening. Using the reporter, single-cell kinetic measurements in a macrophage model system for lysosomal lipid accumulation identified a sub-population of cells that was both significantly lipid deficient and slower to accumulate cholesterol in the lysosomal lumen. In the context of primary monocyte differentiation into macrophages, we discovered that, as the lipid content in the lumen increases, individual lysosomes within single cells accumulate lipids at different rates. Thus, our optical reporter enables quantitative imaging and high-throughput measurement of the lipid content in the endolysosomal lumen of live cells.

Carbon nanotube optical response to lipids

bioRxiv preprint doi: https://doi.org/10.1101/134999; this version posted May 6, 2017. The copyright holder for this preprint (which was not certified by peer review) is the author/funder. All rights reserved. No reuse allowed without permission.

We identified a purified DNA-carbon nanotube complex that responds optically to lipids. Carbon nanotubes were non-covalently functionalized with specific ssDNA oligonucleotides to facilitate separation using ion-exchange chromatography[22], resulting in suspensions of single-chirality DNA-nanotube complexes. The introduction of low density lipoprotein, a biochemical assembly composed of lipids and proteins[23], induced a decrease in emission wavelength (blue shift) that ranged from 0 to 13 nm (Supplementary Fig. 1). The largest solvatochromic response was observed from the (8,6) nanotube spectral band complexed with ss$(GT)_6$, a short oligonucleotide which facilitates separation of the (8,6) species (Supplementary Fig. 2)[22]. The isolated ss$(GT)_6$-(8,6) complex exhibited absorption bands at 730 nm and 1200 nm and a single photoluminescence emission peak at 1200 nm (Fig. 1a, Supplementary Figs. 2b and 3). As measured by atomic force microscopy, the median length of the ss$(GT)_6$-(8,6) complex was 236 nm (Supplementary Fig. 4).

The ss$(GT)_6$-(8,6) complex was characterized by measuring the optical response to several classes of biomolecules and water-soluble lipid analogs. Cholesterol-conjugated polyethylene glycol (PEG), a water-soluble analog of cholesterol, induced a ~ 10 nm decrease in the emission wavelength of the complex at both 2 and 24 hours, while a saturating concentration of BSA, dsDNA from salmon testes, or carboxymethyl cellulose had no measurable effect (Supplementary Fig. 5). The nanotube emission responded immediately to cholesterol-PEG at 2 hours, but at equilibrium, 2 different classes of water-soluble lipid analogs elicited equivalent, large blue shifting responses (Supplementary Fig. 6). The optical response of the ss$(GT)_6$-(8,6) complex was linear over two orders of magnitude of cholesterol concentrations (Fig. 1b). A similar response was observed for both ceramide (Supplementary Fig. 7a) and low-density lipoprotein (LDL), which contains esterified and unesterified cholesterol in their native

bioRxiv preprint doi: https://doi.org/10.1101/134999; this version posted May 6, 2017. The copyright holder for this preprint (which was not certified by peer review) is the author/funder. All rights reserved. No reuse allowed without permission.

conformations (Supplementary Fig. 7b), indicating the general sensitivity of the reporter to both water-soluble lipid analogs and native lipids.

To probe the underlying mechanism governing the response of the ss$(GT)_6$-(8,6) complex, we examined the dependence of emission on the dielectric environment[18]. Using near-infrared hyperspectral microscopy[24], we obtained the emission spectrum from individual surface-adsorbed ss$(GT)_6$-(8,6) complexes in 7 different solvent environments (Supplementary Table 1). The peak emission wavelength of the complexes ranged over 20 nm and exhibited a direct correlation with solvent dielectric constant (Fig. 1c) with a Spearman correlation of 0.89, $p<0.01$). This result suggests that the ss$(GT)_6$-(8,6) complex exhibits a distinct solvatochromic response.

To understand how lipids interact with the surface of ss$(GT)_6$-(8,6) nanotube complexes to induce a solvatochromic shift, we conducted all-atom replica exchange molecular dynamics simulations[25, 26]. First, ss$(GT)_6$ oligonucleotides were equilibrated on the (8,6) nanotube (Supplementary Figs. 8a-b and Supplementary Text) to obtain an equilibrium configuration that exhibited a tight association between the ssDNA and nanotube (Fig. 1d). Cholesterol was then added and equilibrium was reached after 100 ns (Supplementary Fig. 8c). In the resulting configuration, cholesterol bound to exposed regions on the nanotube and induced rearrangement of DNA on the nanotube surface (Supplementary Fig. 9, Supplementary Text). The combined effect was an 18.7% decrease in the density of water molecules within 1.2 nm of the nanotube surface (Fig. 1e). A similar reduction in water density was observed in simulations of sphingomyelin addition to the ss$(GT)_6$-(8,6) complex (Supplementary Fig. 10). The simulations suggest that lipid binding to the ss$(GT)_6$-(8,6) complex reduces the water density on the nanotube surface, thereby lowering the effective local solvent dielectric. As experimentally observed, the

bioRxiv preprint doi: https://doi.org/10.1101/134999; this version posted May 6, 2017. The copyright holder for this preprint (which was not certified by peer review) is the author/funder. All rights reserved. No reuse allowed without permission.

lower dielectric environment corresponds to a blue shift of the nanotube emission wavelength (Fig. 1c).

We further characterized properties of the ss$(GT)_6$-(8,6) optical response to cholesterol. The emission shift on cholesterol addition to surface-adsorbed complexes was rapid (under 2 minutes, limited by the hyperspectral instrument acquisition time, Supplementary Fig. 11a). Sodium deoxycholate, a surfactant and water-soluble cholesterol analog, was added and subsequently removed from the surface-adsorbed complexes, demonstrating that the wavelength shift on analyte binding is intrinsically reversible (Supplementary Fig. 11b). Furthermore, in an acidic environment, the response of the nanotube complex to lipids was similar to that at a neutral pH (Supplementary Fig. 11c).

Localization and biocompatibility in the endolysosomal lumen

We assessed the interaction of ss$(GT)_6$-(8,6) complexes with mammalian cells using near-IR and visible fluorescence microscopy. Macrophages were incubated in complete 10% FBS-supplemented cell culture media with 0.2 µg/mL of ss$(GT)_6$-(8,6) complexes at 37 °C for 30 minutes, before washing with fresh complex-free media. For the experimental conditions used in our experiments, this concentration corresponds to approximately 0.5 picograms of ss$(GT)_6$-(8,6) complexes per cell (calculation in the Methods section). The cells exhibited bright near-IR emission, indicating that nanotubes were strongly associated with the cells (Supplementary Fig. 12). We also measured the uptake of the ss$(GT)_6$-(8,6) complexes as a function of temperature, and quantified the nanotube emission intensity associated with cells. Incubation at 4 °C resulted in 10-fold lower intensity than incubation at 37 °C (Supplementary Fig. 13), indicating that that complexes had been internalized by the cells via endocytosis. These results are consistent with

bioRxiv preprint doi: https://doi.org/10.1101/134999; this version posted May 6, 2017. The copyright holder for this preprint (which was not certified by peer review) is the author/funder. All rights reserved. No reuse allowed without permission.

previous reports of the energy-dependent uptake of ssDNA-nanotube complexes[27] via endocytosis[28, 29]. Additionally, the 236 nm median length of the ss$(GT)_6$-(8,6) complex is comparable to a previously reported optimal length of 320 nm for ssDNA-nanotube uptake by cells[30]. The nanotube emission, quantified from over 700 individual cells incubated with the complex at 37 °C, followed a normal distribution, suggesting a relatively homogeneous uptake of the ss$(GT)_6$-(8,6) complexes by the cells (Supplementary Fig. 14).

To determine the localization of ss$(GT)_6$-(8,6) complexes following uptake, we conducted a series of imaging experiments in macrophages (RAW 264.7 and bone-marrow derived monocytes) and epithelial (U2OS) cells. The ss$(GT)_6$ oligonucleotide was covalently labeled with the visible fluorophores (Cy3, Cy5, or Alexa-647) to prepare fluorophore-labeled ss$(GT)_6$-nanotube complexes. Following internalization of the complexes by macrophages, we acquired emission from the Cy3 dye and nIR emission from the nanotubes in the same imaging field. The colocalization between the signals, observed on two different detectors, indicates that emission from a fluorophore conjugated to the ssDNA on the nanotube is a reliable indicator of nanotube location (Supplementary Fig. 15). Next, we colocalized the fluorescent complexes with Lysotracker Green, a fluorescent probe which accumulates in late endosomes and lysosomes (Supplementary Fig. 16). A quantitative analysis using an unbiased auto-thresholding approach indicated significant colocalization between the Cy5 and Lysotracker Green emission (Pearson coefficient of 0.92 ± 0.01, Manders split colocalization coefficient of 0.95), suggesting that the nanotube signal was contained within LE/Ly. Concomitantly, the nIR emission from the nanotubes localized to the same regions of the cell as the visible emission from Lysotracker, further supporting the endolysosomal localization of the nanotubes (Supplementary Fig. 17). To assess the localization of the nanotubes within individual LE/Ly, we pulsed the cells with

bioRxiv preprint doi: https://doi.org/10.1101/134999; this version posted May 6, 2017. The copyright holder for this preprint (which was not certified by peer review) is the author/funder. All rights reserved. No reuse allowed without permission.

fluorescent (TMR) 10,000 MW dextran, a polymer which accumulates in the lysosomal lumen and does not degrade[31]. Following overnight incubation, the cells were maintained in dextran-free media for 3 hours, before Alexa-647 labeled nanotube complexes were introduced to the cell media for 30 minutes. After washing away free complexes, we performed high magnification confocal microscopy in the live cells. An analysis of over 40 cells (Supplementary Fig. 18a) indicates a 50% colocalization, suggesting that within an hour following their addition, the nanotubes had been transported to the dextran-loaded lysosomes. We extracted line intensity profiles of TMR and Alexa 647 emission and fit them with Gaussian functions (Supplementary Fig. 18b). The single Gaussian intensity distributions of both fluorophores overlapped significantly, with centers that colocalized with diffraction-limited resolution. This result suggests that the nanotubes localized to the same region of the lysosomes as dextran, which is known to remain in the lysosomal lumen[31].

As single-walled carbon nanotubes, composed of only one layer of cylindrical graphene, do not have sufficient electron density to be visible by TEM in cells, we used gold-labeled DNA-nanotube complexes to perform the first incidence of gold-enhanced TEM imaging of individualized SWCNTs in mammalian cells. Citrate-capped gold nanoparticles (~ 10 nm diameter) were conjugated to thiolated ssDNA-nanotube complexes[32]. Unbound gold nanoparticles were removed via centrifugation. Images of the gold nanoparticle-nanotube complexes (Au-SWCNT) deposited directly onto a TEM grid (Supplementary Fig. 19a) confirmed that all gold nanoparticles were attached to carbon nanotubes. We then incubated RAW 264.7 macrophages with 1 mg/L of the gold-labeled nanotubes, and fixed the cells for TEM imaging after removing free gold-nanotube complexes from the solution. In the cells, the gold nanoparticles were clearly visible as dark circles within the late endosomes and lysosomes

bioRxiv preprint doi: https://doi.org/10.1101/134999; this version posted May 6, 2017. The copyright holder for this preprint (which was not certified by peer review) is the author/funder. All rights reserved. No reuse allowed without permission.

(Supplementary Fig. 19b). We quantified the number of gold nanoparticle-nanotubes within each lysosome. An analysis of the relatively frequency distribution suggests that if two AuNP are observed within one LE/Ly, then the two nanoparticles are statistically likely to be linked to each other, most likely via a nanotube (Supplementary Fig. 19c). The images showed that the gold nanoparticles localized to the lysosomal lumen and were not associated with the limiting membrane. The assertion that the nanotube interacts negligibly with the limiting lysosomal membrane is also supported by the fact that the persistence length of the (8,6) chirality nanotube is >50 μm[33], and the ss$(GT)_6$-(8,6) complex has an average length of 236 nm (Supplementary Fig. 4), implying that the highly curved limiting membrane of the lysosome would make little contact with the linear nanotube.

To determine long-term fate of the complexes, we acquired nIR movies of ss$(GT)_6$-(8,6) complexes within macrophages at 6, 24 and 48 hours after the initial 30 minute incubation (Supplementary Videos 1, 2, and 3). At each time point, emission from the complexes exhibited both passive diffusion and directed, linear movements consistent with the active transport of lysosomes along microtubules[34], suggesting that the nanotube complexes remain within late endosomes and lysosomes. The emerging view, from our series of experiments, indicates the efficient uptake of DNA-nanotube complexes via endocytosis, rapid transport to the late endosomes and lysosomes, and stable localization to the lysosomal lumen.

We next assessed the effects of the DNA-nanotube complexes (at 1 mg/L, 5 times higher than the working concentration) on lysosomal morphology and function. Gold-conjugated DNA-nanotube complexes were incubated with RAW 267.4 cells for 30 minutes before fixing and preparing for TEM imaging. Analysis of LE/Ly size, diameter and aspect ratio from the TEM images show no statistical differences between control macrophages and macrophages incubated

bioRxiv preprint doi: https://doi.org/10.1101/134999; this version posted May 6, 2017. The copyright holder for this preprint (which was not certified by peer review) is the author/funder. All rights reserved. No reuse allowed without permission.

with 1 mg/L complexes (Supplementary Fig. 20). LE/Ly in which gold-nanotubes were explicitly detected also displayed similar morphology to controls (Supplementary Fig. 21). At this elevated concentration of complexes (1 mg/L), we did not observe a change in cell viability and proliferation (Supplementary Fig. 22). We also investigated effects of the nanotubes on the ability of the LE/Ly to maintain a pH gradient (Supplementary Fig. 23), and on lysosomal membrane permeabilization (Supplementary Fig. 24) with single-organelle resolution, resulting in no measurable changes.

Detecting lipid accumulation in the endolysosomal lumen of live cells

We investigated whether ss$(GT)_6$-(8,6) complexes, localized in the lumen of late endosomes and lysosomes of live cells, could optically detect lipid accumulation in their environment. RAW 264.7 macrophages were incubated with the complexes for 30 minutes in complete 10% serum-supplemented media at 37° C and washed with fresh media. To induce lysosomal accumulation of free cholesterol, we prepared cells that were pre-treated with U18666A[35], a compound that inhibits the action of Niemann-Pick C1[36], a membrane protein that effluxes free cholesterol out of the lysosomes, to mimic the Niemann-Pick C1 disease phenotype. Cells were also pre-treated with Lalistat[37], an inhibitor of lysosomal acid lipase (LAL), which is the central enzyme that hydrolyzes low density lipoproteins[38]. Inhibition of LAL leads to the accumulation of esterified cholesterol, which is observed in Wolman's disease.

Using near-IR hyperspectral microscopy, we acquired the emission from the complexes localized within the LE/Ly of macrophages under these three conditions (Fig. 1f). When the emission wavelength is mapped to a color-scale and overlaid on a transmitted light image, the spatially-resolved emission from ss$(GT)_6$-(8,6) complexes resulted in live-cell maps of endolysosomal

bioRxiv preprint doi: https://doi.org/10.1101/134999; this version posted May 6, 2017. The copyright holder for this preprint (which was not certified by peer review) is the author/funder. All rights reserved. No reuse allowed without permission.

lipid content (Supplementary Fig. 25). The mean emission blue-shift for the two drug-treated conditions was over 11 nm compared with the control, with a single population for all three conditions, indicating lipid accumulation in all LE/Ly that contained the complexes (Fig. 1g). Neither Lalistat or U18666A directly perturbed the emission wavelength of the complexes (Supplementary Fig. 26). The endolysosomal lipid maps thus reflect the optical response of the complexes to the accumulation of both free and esterified cholesterol in the endolysosomal lumen.

We asked whether DNA-nanotube complexes altered low-density lipoprotein (LDL) processing through the LE/Ly. Using lipid biochemical assays, we detected no measurable differences in the cholesterol or total lipid content of endolysosomal fractions containing the complexes (Supplementary Fig. 27). We also assessed the LDL receptor (LDLr) levels in cells via western blots (Supplementary Fig. 28) and observed no perturbation in cells containing DNA-nanotube complexes. Lipoprotein hydrolysis and cholesterol efflux within the lysosomes were measured using fluorophore-labeled acetylated LDL (Supplementary Fig. 29) and LipidTox (Supplementary Fig. 30) respectively, with no measurable effect conferred by the complexes.

We quantified the nanotube emission response as a function of loading concentration. At a 5-fold dilution of the working concentration, the response of the emission wavelength to U81666A-induced lipid accumulation did not change, indicating that the function of the ss$(GT)_6$-(8,6) complex was stable over a range of concentrations (Supplementary Fig. 31).

Based on the findings from our experiments, we present a model for the optical response of ss$(GT)_6$-(8,6) ssDNA-nanotube complexes in live cells under the conditions investigated (Fig. 1h). The complexes enter the endolysosomal pathway and localize within the lumen of late

bioRxiv preprint doi: https://doi.org/10.1101/134999; this version posted May 6, 2017. The copyright holder for this preprint (which was not certified by peer review) is the author/funder. All rights reserved. No reuse allowed without permission.

endosomes and lysosomes (LE/Ly). In the complex environment of the lysosomal lumen, the nanotube emission functions as a cell-specific spectral fingerprint for the lipid content. Upon dysfunction of the NPC1 protein via introduction of U18666A to cells, free cholesterol (FC) accumulates within the lumen of the LE/Ly and adsorbs to the surface of the ss$(GT)_6$-(8,6) complex, resulting in a distinct blue-shifting response of the nanotube emission. Similarly, upon introduction of Lalistat to cells, cholesteryl esters (CE) accumulate in the lysosomal lumen, resulting in the adsorption of CE to the nanotube surface, and a concomitant blue-shifting response. In both situations, multiple secondary lipids also accumulate in the lysosomal lumen[39]. Hence, we find that the ss$(GT)_6$-(8,6) DNA-nanotube complex functions as a quantitative optical reporter of lipid accumulation in the endolysosomal lumen via solvatochromic shifting of intrinsic carbon nanotube photoluminescence. Henceforth, we refer to ss$(GT)_6$-(8,6) as the 'reporter'.

As the nanotube emission is exclusively from the endolysosomal lumen, we investigated whether the nanotube spectra alone, obtained without imaging, could function as an analytical tool to benchmark drug-induced endolysosomal lipid accumulation in a high-throughput format. Using a customized nIR spectrometer[40], we obtained spectra from complexes within live RAW 264.7 macrophages (Fig. 1i) and detected a 9 nm shift in the emission from cells treated with U18666A –an example of a cationic amphiphilic drug which induces DIPL[41] (Fig. 1j). These results were statistically similar to the hyperspectral data of control and U18666A-treated macrophages (Fig. 1k), indicating the amenability of the complexes for both imaging and a spectroscopy-based assay which facilitates higher throughput.

Lipid flux and heterogeneity in lysosomal storage disorders

bioRxiv preprint doi: https://doi.org/10.1101/134999; this version posted May 6, 2017. The copyright holder for this preprint (which was not certified by peer review) is the author/funder. All rights reserved. No reuse allowed without permission.

The reporter was assessed for its response in primary cells from a patient with Niemann-Pick type C (NPC), a lysosomal storage disease characterized by a massive accumulation of unesterified cholesterol in the lysosomes[42, 43]. Fibroblasts collected from the NPC patient, as well as wild-type (WT) human fibroblasts, were incubated with the reporter for 30 minutes, then rinsed, and incubated in fresh media. Hyperspectral data collected after 24 hours indicates that the reporter blue-shifted by an average of 6 nm in NPC1 human fibroblasts, compared to WT human fibroblasts (Fig. 2a). The lipid content of WT fibroblast lysosomes was relatively homogeneous, as evinced by the narrow distribution of the reporter emission (Fig. 2b). In contrast, the reporter exhibited a broad emission profile within NPC1 cells, confirming the published findings that NPC1 cells exhibit a wide distribution of lipid concentrations[44]. The histogram also suggests that a sizeable fraction of lysosomes contain near-normal cholesterol content.

We measured the emission from the reporter in NPC1 fibroblasts treated with hydroxypropyl-β-cyclodextrin (HPβCD), a drug known to facilitate the efflux of accumulated cholesterol from the lysosomal lumen[37]. After HPβCD treatment (100 μM) for 24 hours, hyperspectral imaging revealed significant red-shifting of the reporter emission from the same NPC1 cells that were previously blue-shifted (Fig. 2a). The distribution of reporter emission from the HPβCD-treated NPC1 fibroblasts appeared notably similar to the emission from WT fibroblasts (Fig. 2b), and reduction of total cell cholesterol content was confirmed by fixing the cells and staining with filipin (Fig. 2c). Filipin staining was more pronounced in NPC1 fibroblasts as compared to WT fibroblasts, and HPβCD treatment resulted in significantly diminished filipin signal in NPC1 cells (Supplementary Fig. 32), thus validating the results obtained from the reporter alone. Unlike the reporter, however, Filipin staining could not resolve heterogeneity in the lysosomal

bioRxiv preprint doi: https://doi.org/10.1101/134999; this version posted May 6, 2017. The copyright holder for this preprint (which was not certified by peer review) is the author/funder. All rights reserved. No reuse allowed without permission.

lipid content. Additionally, pre-treatment of NPC1 fibroblasts with HPβCD prevented the blue-shifting of the reporter (Supplementary Fig. 33). Thus, the reporter responded to treatment both via reversal of the response and prevention of the initial response to lysosomal lipid accumulation.

Lysosomal lipids in differentiating bone marrow-derived monocytes

Atherosclerosis is driven by lipoprotein-derived cholesterol accumulation by differentiating monocyte-macrophages[45]. We employed the reporter to measure lysosomal lipid content during the process of bone marrow-derived monocyte differentiation into bone marrow-derived macrophages (BMDMs). Bone marrow-derived monocytes, isolated from C57BL/6 mice, were cultured in the presence of colony stimulating factor-1 (CSF1) for 7 days to induce differentiation into macrophages[46]. The differentiation process was verified by the increase in the fraction of cells expressing the macrophage markers Cd11b and F4/80, and a decrease in the fraction of cells expressing the monocytic/granulocytic marker Gr-1 (Fig. 3a, Supplementary Fig. 34)[47]. Following incubation of the BMDMs with the reporter for 30 minutes, free reporter was rinsed away and the cells were incubated for an additional 6 hours in CSF-1 containing cell culture media. Endolysosomal lipid maps generated from BMDMs after 3 and 5 days of maturation were strikingly different (Fig. 3b). As seen in the histogram of the mean reporter emission from individual cells, the reporter blue-shifted by approximately 5 nm between day 3 and day 5 of maturation (Fig. 3c), indicating that accumulation of lipids in the lysosomal lumen accompanied the macrophage differentiation in this timeframe. We confirmed this finding in 4 separate animals with 10 technical replicates each (Fig. 3d). Native LDL is taken up by macrophages differentiated with CSF-1[48] and results in cholesterol accumulation within the cell[49]. Although the lipid content within the LE/Ly is not precisely known, the blue-shift in the

bioRxiv preprint doi: https://doi.org/10.1101/134999; this version posted May 6, 2017. The copyright holder for this preprint (which was not certified by peer review) is the author/funder. All rights reserved. No reuse allowed without permission.

reporter emission indicates that the reporter is sensitive to non-pathological increases in lysosomal lipid content.

We used hyperspectrally-generated maps to quantify the intracellular heterogeneity of lipid content within individual lysosomes of single BMDM cells (Fig. 4a). Hyperspectral images of two cells (Fig. 4b) from the bone marrow-derived monocyte population on day 3 of differentiation showed distinctly different intracellular heterogeneity of the reporter response, evident from the histogram widths (Fig. 4c). To mathematically quantify the intracellular heterogeneity of reporter emission within each cell, we used the normalized Simpson's Index (nSI, Supplementary Methods), a statistical measure of diversity[50, 51]. For the cells shown in Fig. 4b, the nSIs were significantly different (Cell 1 nSI = 0.18, Cell 2 nSI = 0.74). By plotting the mean reporter emission wavelength and nSI for a large population of cells on day 3, cells with the most lipid-rich lysosomes (shorter wavelength) exhibited greater intracellular heterogeneity in lysosomal lipid contents (Fig. 4d, Spearman correlation of 0.33, $p < 0.01$, for $n = 64$ cells). This observation, confirmed in BMBMs isolated from 4 different mice (Supplementary Fig. 35), suggests that within differentiating monocytes, cells with lipid-rich lysosomes maintain a sub-population of lysosomes that are relatively lipid-deficient.

Single-cell kinetic measurements of lipid accumulation

The kinetics of lipid accumulation in the lysosomal lumen of live macrophages were investigated on a single-cell level. In RAW 264.7 macrophages cultured in media containing LPDS, the initial reporter emission was approximately 1200 nm. After introducing both acLDL and U18666A to the cell media, we acquired hyperspectral images every 10 minutes for a total time course of 2 hours (Fig. 5a). Single-cell emission trajectories were computed for all cells with reporter peak

bioRxiv preprint doi: https://doi.org/10.1101/134999; this version posted May 6, 2017. The copyright holder for this preprint (which was not certified by peer review) is the author/funder. All rights reserved. No reuse allowed without permission.

emission intensities of over 4 times higher than the background. The mean reporter emission from individual cells blue-shifted and reached equilibrium over approximately 90 minutes (Fig. 5b). For each cell, the spectral trajectories were fit with a single exponential function to obtain the time constant, time lag, and the starting and final reporter wavelengths (Supplementary Fig. S36). The time constants of lipid accumulation in the cells averaged approximately 40 minutes and followed a lognormal distribution (Fig. 5c). One potential explanation for this finding is that a lognormal distribution is often observed for a quantity arising from multiple serial processes[52]. We believe that this distribution of time constants from individual cells is consistent with the process of lysosomal lipid accumulation, which involves sequential processes including LDL uptake into the early endosome, delivery of LDL to the lysosome, hydrolysis of esterified cholesterol by LAL, and the inhibited transfer of free cholesterol from NPC2 to NPC1.

Interestingly, the distribution of time constants showed marked heterogeneity, with the slowest and fastest time constants differing by an order of magnitude. Cells exhibiting slower rates of lipid accumulation also exhibited an initial state of relative lipid deficiency. The time constant of lipid accumulation modestly correlated with the starting wavelength (Spearman correlation of 0.33, $p<0.01$). Notably, the slowest shifting cells (defined as cells with a time constant > 90 minutes) exhibited an initial average emission wavelength >1202 nm, 2 nm more red-shifted than the faster shifting cells (Fig. 5d). This result suggests the existence of a subpopulation of cells that maintained both lipid-deficient lysosomes and an extremely slow rate of lipid accumulation; i.e. these individual cells in the population may be especially resistant to lysosomal lipid accumulation.

Conclusion

bioRxiv preprint doi: https://doi.org/10.1101/134999; this version posted May 6, 2017. The copyright holder for this preprint (which was not certified by peer review) is the author/funder. All rights reserved. No reuse allowed without permission.

In this work, we developed a carbon nanotube optical reporter, composed of the (8,6) SWCNT species non-covalently complexed with a short DNA oligonucleotide, that can function as an optical reporter of lipid content within the endolysosomal lumen of live cells. The near-infrared photoluminescence of the nanotube responds quantitatively to lipids in the local environment of the reporter via shifting of the nanotube optical bandgap. Experimental evidence and all-atom molecular dynamics simulations suggest that the mechanism of the response is solvatochromic shifting due to the reduction in water density on the nanotube surface. The reporter remains within the endocytic pathway and localizes to the lumen of late endosomes and lysosomes, where its near-infrared emission responds rapidly and reversibly to lipid accumulation in the lumen. Via nIR hyperspectral microscopy, the reporter can qualitatively map lipids in live cells with single-cell and single-organelle resolution. Using spectroscopy only, the reporter can measure lysosomal lipid accumulation in live cells in a high-throughput drug screening-type format. The reporter detected lipid accumulation in lysosomal storage disorders, including in the lysosomes of fibroblasts derived from a patient with Niemann-Pick Type C, as well as phenotypic reversal in the same cells after drug treatment. Lysosomal lipid accumulation in differentiating bone marrow-derived monocytes was observed, and high resolution endolysosomal lipid maps revealed intracellular heterogeneity in the form of a sub-population of lipid-deficient LE/Ly in lipid-rich cells. Using the reporter to observe single cell kinetics of modified LDL accumulation within the lysosomes, we found that the rate of cholesterol accumulation differed by an order of magnitude across macrophages. As the first technique for measuring lipid flux in the lysosomal lumen of live cells, we expect this tool will have broad utility in the investigation of disease pathways associated with altered lipid biology.

bioRxiv preprint doi: https://doi.org/10.1101/134999; this version posted May 6, 2017. The copyright holder for this preprint (which was not certified by peer review) is the author/funder. All rights reserved. No reuse allowed without permission.

References:

1. Xu, H. & Ren, D. Lysosomal physiology. *Annu. Rev. Physiol.* **77**, 57-80 (2015).
2. Parenti, G., Andria, G. & Ballabio, A. Lysosomal storage diseases: from pathophysiology to therapy. *Annual review of medicine* **66**, 471-486 (2015).
3. Grayson, M. Lysosomal storage disorders. *Nature* **537**, S145-S145 (2016).
4. Jerome, W.G. Lysosomes, cholesterol and atherosclerosis. *Clin. Lipidol.* **5**, 853-865 (2010).
5. Bieghs, V. et al. Trapping of oxidized LDL in lysosomes of Kupffer cells is a trigger for hepatic inflammation. *Liver Int.* **33**, 1056-1061 (2013).
6. Nixon, R.A. The role of autophagy in neurodegenerative disease. *Nat. Med.* **19**, 983-997 (2013).
7. Kirkegaard, T. & Jäättelä, M. Lysosomal involvement in cell death and cancer. *Biochim Biophys Acta.* **1793**, 746-754 (2009).
8. Glock, M., Muehlbacher, M., Hurtig, H., Tripal, P. & Kornhuber, J. Drug-induced phospholipidosis caused by combinations of common drugs in vitro. *Toxicol in Vitro* **35**, 139-148 (2016).
9. Shayman, J.A. & Abe, A. Drug induced phospholipidosis: An acquired lysosomal storage disorder. *BBA-MOL. CELL BIOL. L.* **1831**, 602-611 (2013).
10. Maxfield, F.R. & Wüstner, D. in Methods in Cell Biology, Vol. 108 367-393 (Academic Press, 2012).
11. Haberkant, P. & Holthuis, J.C. Fat & fabulous: bifunctional lipids in the spotlight. *Biochimica et biophysica acta* **1841**, 1022-1030 (2014).
12. Hofmann, K. et al. A novel alkyne cholesterol to trace cellular cholesterol metabolism and localization. *J. Lipid. Res.* **55**, 583-591 (2014).
13. Takatori, S., Mesman, R. & Fujimoto, T. Microscopic methods to observe the distribution of lipids in the cellular membrane. *Biochemistry* **53**, 639-653 (2014).
14. Kucherak, O.A. et al. Switchable Nile Red-Based Probe for Cholesterol and Lipid Order at the Outer Leaflet of Biomembranes. *J. Am. Chem. Soc.* **132**, 4907-4916 (2010).
15. Darwich, Z., Klymchenko, A.S., Dujardin, D. & Mely, Y. Imaging lipid order changes in endosome membranes of live cells by using a Nile Red-based membrane probe. *RSC Adv.* **4**, 8481-8488 (2014).
16. O'Connell, M.J. et al. Band gap fluorescence from individual single-walled carbon nanotubes. *Science* **297**, 593-596 (2002).
17. Barone, P.W., Baik, S., Heller, D.A. & Strano, M.S. Near-infrared optical sensors based on single-walled carbon nanotubes. *Nat. Mater.* **4**, 86-92 (2005).
18. Larsen, B.A. et al. Effect of solvent polarity and electrophilicity on quantum yields and solvatochromic shifts of single-walled carbon nanotube photoluminescence. *J. Am. Chem. Soc.* **134**, 12485-12491 (2012).
19. Choi, J.H. & Strano, M.S. Solvatochromism in single-walled carbon nanotubes. *Appl. Phys. Lett.* **90** (2007).
20. Heller, D.A. et al. Optical detection of DNA conformational polymorphism on single-walled carbon nanotubes. *Science* **311**, 508-511 (2006).
21. Heller, D.A. et al. Multimodal optical sensing and analyte specificity using single-walled carbon nanotubes. *Nat. Nano.* **4**, 114-120 (2009).

bioRxiv preprint doi: https://doi.org/10.1101/134999; this version posted May 6, 2017. The copyright holder for this preprint (which was not certified by peer review) is the author/funder. All rights reserved. No reuse allowed without permission.

22. Tu, X., Manohar, S., Jagota, A. & Zheng, M. DNA sequence motifs for structure-specific recognition and separation of carbon nanotubes. *Nature* **460**, 250-253 (2009).
23. Orlova, E.V. et al. Three-dimensional structure of low density lipoproteins by electron cryomicroscopy. *Proc. Natl. Acad. Sci. USA* **96**, 8420-8425 (1999).
24. Roxbury, D. et al. Hyperspectral microscopy of near-infrared fluorescence enables 17-chirality carbon nanotube imaging. *Sci. Rep.* **5** (2015).
25. Humphrey, W., Dalke, A. & Schulten, K. VMD: Visual molecular dynamics. *J. Mol. Graph.* **14**, 33-38 (1996).
26. Sugita, Y. & Okamoto, Y. Replica-exchange molecular dynamics method for protein folding. *Chem. Phys. Lett.* **314**, 141-151 (1999).
27. Cherukuri, P., Bachilo, S.M., Litovsky, S.H. & Weisman, R.B. Near-infrared fluorescence microscopy of single-walled carbon nanotubes in phagocytic cells. *J. Am. Chem. Soc.* **126**, 15638-15639 (2004).
28. Heller, D.A., Baik, S., Eurell, T.E. & Strano, M.S. Single-walled carbon nanotube spectroscopy in live cells: Towards long-term labels and optical sensors. *Adv. Mater.* **17**, 2793-+ (2005).
29. Bhattacharya, S., Roxbury, D., Gong, X., Mukhopadhyay, D. & Jagota, A. DNA Conjugated SWCNTs Enter Endothelial Cells via Rac1 Mediated Macropinocytosis. *Nano Lett.* **12**, 1826-1830 (2012).
30. Jin, H., Heller, D.A., Sharma, R. & Strano, M.S. Size-dependent cellular uptake and expulsion of single-walled carbon nanotubes: single particle tracking and a generic uptake model for nanoparticles. *Acs Nano* **3**, 149-158 (2009).
31. Kilpatrick, B.S., Eden, E.R., Hockey, L.N., Futter, C.E. & Patel, S. Methods for monitoring lysosomal morphology. *Method Cell Biol* **126**, 1-19 (2015).
32. Han, X.G., Li, Y.L. & Deng, Z.X. DNA-wrapped single-walled carbon nanotubes as rigid templates for assembling linear gold nanoparticle arrays. *Adv. Mater.* **19**, 1518-+ (2007).
33. Fakhri, N., Tsyboulski, D.A., Cognet, L., Weisman, R.B. & Pasquali, M. Diameter-dependent bending dynamics of single-walled carbon nanotubes in liquids. *Proc. Natl. Acad. Sci. USA* **106**, 14219-14223 (2009).
34. Bandyopadhyay, D., Cyphersmith, A., Zapata, J.A., Kim, Y.J. & Payne, C.K. Lysosome transport as a function of lysosome diameter. *Plos One* **9** (2014).
35. Liscum, L. & Faust, J.R. The intracellular transport of low density lipoprotein-derived cholesterol is inhibited in Chinese hamster ovary cells cultured with 3-β-[2-(diethylamino)ethoxy]androst-5-en-17-one. *J. Biol. Chem.* **264**, 11796-11806 (1989).
36. Lu, F. et al. Identification of NPC1 as the target of U18666A, an inhibitor of lysosomal cholesterol export and Ebola infection. *eLife* **4** (2015).
37. Rosenbaum, A.I., Zhang, G., Warren, J.D. & Maxfield, F.R. Endocytosis of beta-cyclodextrins is responsible for cholesterol reduction in Niemann-Pick type C mutant cells. *Proc. Natl. Acad. Sci. USA* **107**, 5477-5482 (2010).
38. Sloan, H.R. & Fredrickson, D.S. Enzyme deficiency in cholesteryl ester storage idisease. *J. Clin. Invest.* **51**, 1923-1926 (1972).
39. Walkley, S.U. & Vanier, M.T. Secondary lipid accumulation in lysosomal disease. *Bba-Mol Cell Res* **1793**, 726-736 (2009).
40. Roxbury, D., Jena, P.V., Shamay, Y., Horoszko, C.P. & Heller, D.A. Cell Membrane Proteins Modulate the Carbon Nanotube Optical Bandgap via Surface Charge Accumulation. *ACS Nano* **10**, 499-506 (2016).

bioRxiv preprint doi: https://doi.org/10.1101/134999; this version posted May 6, 2017. The copyright holder for this preprint (which was not certified by peer review) is the author/funder. All rights reserved. No reuse allowed without permission.

41. Halliwell, W.H. Cationic amphiphilic drug-induced phospholipidosis. *Toxicol Pathol* **25**, 53-60 (1997).
42. Carstea, E.D. et al. Niemann-Pick C1 disease gene: Homology to mediators of cholesterol homeostasis. *Science* **277**, 228-231 (1997).
43. Maxfield, F.R. & Tabas, I. Role of cholesterol and lipid organization in disease. *Nature* **438**, 612-621 (2005).
44. Linder, M.D. et al. Rab8-dependent recycling promotes endosomal cholesterol removal in normal and sphingolipidosis cells. *Mol. Biol. Cell* **18**, 47-56 (2007).
45. Moore, K.J., Sheedy, F.J. & Fisher, E.A. Macrophages in atherosclerosis: a dynamic balance. *Nat Rev Immunol* **13**, 709-721 (2013).
46. Pyonteck, S.M. et al. CSF-1R inhibition alters macrophage polarization and blocks glioma progression. *Nat. Med.* **19**, 1264-1272 (2013).
47. Akkari, L. et al. Distinct functions of macrophage-derived and cancer cell-derived cathepsin Z combine to promote tumor malignancy via interactions with the extracellular matrix. *Genes Dev.* **28**, 2134-2150 (2014).
48. Anzinger, J. et al. Native low-density lipoprotein uptake by Macrophage Colony-Stimulating Factor-differentiated human macrophages is mediated by macropinocytosis and micropinocytosis. *J Immunol* **184** (2010).
49. Zhao, B. et al. Constitutive receptor-independent low density lipoprotein uptake and cholesterol accumulation by macrophages differentiated from human monocytes with macrophage-colony-stimulating factor (M-CSF). *J. Biol. Chem.* **281**, 15757-15762 (2006).
50. Simpson, E.H. Measurement of diversity. *Nature* **163**, 688 (1949).
51. Hunter, P.R. & Gaston, M.A. Numerical index of the discriminatory ability of typing systems: An application of Simpson's index of diversity. *J. Clin. Microbiol.* **26**, 2465-2466 (1988).
52. Koch, A.L. The logarithm in biology - Mechanisms generating the log-normal distribution exactly. *J Theor Biol* **12**, 276-290 (1966).

bioRxiv preprint doi: https://doi.org/10.1101/134999; this version posted May 6, 2017. The copyright holder for this preprint (which was not certified by peer review) is the author/funder. All rights reserved. No reuse allowed without permission.

Methods:

DNA encapsulation of single-walled carbon nanotubes

The chemical reagents were purchased from Sigma-Aldrich (St. Louis, MO, US) and Fisher Scientific (Pittsburgh, US). Single-walled carbon nanotubes (SWCNTs) produced by the HiPco process were used throughout the study (Unidym, Sunnyvale, CA). The carbon nanotubes were dispersed with DNA oligonucleotides via probe-tip ultrasonication (Sonics & Materials, Inc.) of 2 mg of the specified oligonucleotide (IDT DNA, Coralville, IA) with 1 mg of raw SWCNT in 1 mL of 0.1 M NaCl for 30 minutes at 40% of the maximum amplitude of the ultrasonicator (SONICS Vibra Cell). Following ultrasonication, the dispersions were ultracentrifuged (Sorvall Discovery 90SE) for 30 minutes at 280,000 x *g*. The top ¾ of the resultant supernatant was collected and its concentration was determined with a UV/Vis/nIR spectrophotometer (Jasco, Tokyo, Japan) using the extinction coefficient Abs_{910} = 0.02554 L $mg^{-1}cm^{-1}$ [24]. To remove free DNA, 100 kDa Amicon centrifuge filters (Millipore) were used to concentrate and re-suspend the DNA-nanotube complexes.

Purification of single-chirality nanotube complexes

Carbon nanotubes were separated by an ion-exchange chromatography (IEX) method according to the procedure described by Tu et al[22]. Briefly, unsorted HiPco nanotubes were dispersed using a DNA oligonucleotide with the sequence ss$(GT)_6$, as described above. The sample was injected into a high performance liquid chromatograph (HPLC) (Agilent, 1260 Infinity) fitted with an anion-exchange column (Biochrom Labs, Inc., CNT-NS1500) with a running buffer of 2x SSC at a flow rate of 2 mL/min. A linearly increasing salt concentration gradient of 1M NaSCN (5%/min) was used to elute the nanotubes from the stationary phase and fractions were collected. The first fraction exciting the HPLC contained the highest purity of the (8,6) species, estimated at 86%, which was used for subsequent studies.

Near-infrared fluorescence microscopy of single-walled carbon nanotubes

As described in a previous study[24], near infrared fluorescence microscopy was used to acquire the photoluminescence emission from SWCNTs. The system comprised a continuous wave (CW) 730 nm diode laser with an output power of 2 W injected into a multimode fiber to produce the excitation source for fluorescence experiments. To ensure a homogenous illumination over the entire microscope field of view, the excitation beam passed through a custom beam-shaping module to produce a top-hat intensity profile with under 20% power variation on the imaged region of the sample. The final power at the sample was 230 mW. A longpass dichroic mirror with a cut-on wavelength of 875 nm (Semrock) was aligned to reflect the laser to the sample stage of an Olympus IX-71 inverted microscope (with internal optics modified to improve near-infrared transmission from 900-1400 nm) equipped with a 20X LCPlan N, 20X/0.45 IR objective and a UAPON100XOTIRF, 1.49 oil objective (Olympus, USA). Emission was collected with a 2D InGaAs array detector (Photon Etc.). Z-stacks of broadband, widefield emission (from 900 to 1650 nm) were acquired in steps of 0.5 µm, which satisfied the Nyquist sampling criterion for 100X magnification. Custom codes, written using Matlab software, were used to subtract background, correct for non-uniformities in excitation profile, and compensate for dead pixels on the detector. Hyperspectral microscopy was conducted by passing the emission through a volume Bragg grating (VBG) placed immediately before the InGaAs array in the optical path. The filtered image produced on the InGaAs camera

bioRxiv preprint doi: https://doi.org/10.1101/134999; this version posted May 6, 2017. The copyright holder for this preprint (which was not certified by peer review) is the author/funder. All rights reserved. No reuse allowed without permission.

was composed of a series of vertical lines, each with a specific wavelength. The reconstruction of a spatially-rectified image stack was performed using cubic interpolation on every pixel for each monochromatic image, according to the wavelength calibration parameters. The rectification produced a hyperspectral "cube" of images of the same spatial region exhibiting distinct spectral regions with 3.7 nm FHWM bandwidths. Approximately 50% of the emission intensity from the nanotubes is reduced after passage through the VBG.

Analysis and processing of hyperspectral data

Hyperspectral data acquired was saved as a (320 x 256 x 26) 16-bit array, where the first two coordinates signify the spatial location of a pixel and the last coordinate is its position in wavelength space. For the (8,6) nanotube, the 26-frame wavelength space ranges from 1150 nm to 1250 nm. An initial filter removed any pixels with a maximum intensity value outside (1170 to 1220 nm), as these were background pixels that emit outside the range for (8,6). For the remaining pixels, a peak-finding algorithm was used to calculate the intensity range for a given pixel i.e. range = (intensity_maximum – intensity_minimum). A data point was designated as a peak if its intensity was range/4 greater than the intensity of adjacent pixels. Pixels that failed the peak-finding threshold, primarily due to low intensity above the background, were removed from the data sets. The remaining pixels were fit with a Lorentzian function. Fits with $R^2 < 0.8$ were also removed.

Preparation of gold nanoparticle-conjugated nanotubes

Gold nanoparticle-conjugated nanotubes were prepared according to a previously published study. Briefly, 10 nm citrate-capped gold nanoparticles were synthesized by bringing 50 mL of 0.01 wt% HAuCl4 and adding 2 mL of 1 wt% Sodium(III) citrate. After 2 minutes, the solution turns bright red, indicating nanoparticle formation. The gold nanoparticles were stabilized via a ligand exchange reaction by shaking overnight with bis(p-sulfonatophenyl)phenylphosphine dihydrate dipotassium salt. The nanoparticles were then centrifuged and resuspended in deionized water. In parallel, ss(GT)27-T6-thiol-dispersed HiPco nanotube complexes were created by means of the previously described sonication and centrifugation protocol. The nanotube complexes were filtered with ultracentrifuge filters three times to remove unbound DNA. The nanotube complexes and excess gold nanoparticles were then shaken overnight. The unbound gold nanoparticles were removed via centrifugation, which would pellet the unbound nanoparticles, and careful supernatant extraction.

Transmission electron microscopy (TEM) imaging

Gold nanoparticle-nanotube conjugates were first imaged on carbon coated TEM grids by letting a 20 µL drop evaporate in the center of the grid. For imaging in RAW 264.7 cells, gold nanoparticle-nanotubes were introduced to the media for 30 minutes at 1 mg/L, and then washed thoroughly and replaced with fresh media. After 6 hours, cells were washed with serum-free media then fixed with a modified Karmovsky's fix of 2.5% glutaraldehyde, 4% paraformaldehye and 0.02% picric acid in 0.1M sodium cacodylate buffer at pH 7.2. Following a secondary fixation in 1% osmium tetroxide and 1.5% potassium ferricyanide, samples were dehydrated through a graded ethanol series, and embedded in an epon analog resin. Ultrathin sections were cut using a Diatome diamond knife (Diatome, USA, Hatfield, PA) on a Leica Ultracut S ultramicrotome (Leica, Vienna, Austria). Sections were collected on copper grids and further

bioRxiv preprint doi: https://doi.org/10.1101/134999; this version posted May 6, 2017. The copyright holder for this preprint (which was not certified by peer review) is the author/funder. All rights reserved. No reuse allowed without permission.

contrasted with lead citrate and viewed on a JEM 1400 electron microscope (JEOL, USA, Inc., Peabody, MA) operated at 120 kV. Images were recorded with a Veleta 2K x2K digital camera (Olympus-SIS, Germany).

Fluorescence microscopy of live cells

Standard fluorescence imaging in the UV-visible emission range was performed on the hyperspectral microscope by using an XCite Series 120Q lamp as the light source and a QiClick CCD camera (QImaging) directly attached to a c-mount on a separate port of the microscope. Fluorescence filter sets from Chroma Technology and Semrock were used. Confocal imaging was performed on a Zeiss LSM 880, AxioObserver microscope equipped with a Plan-Apochromat 63× Oil 1.4 NA differential interference contrast (DIC) M27 objective in a humidified chamber at 37 °C. Z-stacks were obtained using a step size of 198-220 nm.

Fluorescence spectroscopy of carbon nanotubes in solution

Fluorescence emission spectra from aqueous solutions of SWCNTs were acquired using a home-built apparatus consisting of a tunable white light laser source, inverted microscope, and InGaAs nIR detector[40]. The SuperK EXTREME supercontinuum white light laser source (NKT Photonics) was used with a VARIA variable bandpass filter accessory capable of tuning the output 500 – 825 nm with a bandwidth of 20 nm. During the course of the measurements, the excitation wavelength remained at 730 nm, close to the resonant excitation maximum of the DNA-encapsulated (8,6) nanotube species. The light path was shaped and fed into the back of an inverted IX-71 microscope (Olympus) where it passed through a 20x nIR objective (Olympus) and illuminated a 100 µL nanotube sample at a concentration of 0.2 mg/L in a 96-well plate (Corning). With an exposure time of 1 second, the emission from the nanotube sample was collected through the 20x objective and passed through a dichroic mirror (875 nm cutoff, Semrock). The light was f/# matched to the spectrometer using several lenses and injected into an Isoplane spectrograph (Princeton Instruments) with a slit width of 410 µm which dispersed the emission using a 86 g/mm grating with 950 nm blaze wavelength. The spectral range was 930 – 1369 nm with a resolution of ~0.7 nm. The light was collected by a PIoNIR InGaAs 640 x 512 pixel array (Princeton Instruments). A HL-3-CAL-EXT halogen calibration light source (Ocean Optics) was used to correct for wavelength-dependent features in the emission intensity arising from the spectrometer, detector, and other optics. A Hg/Ne pencil style calibration lamp (Newport) was used to calibrate the spectrometer wavelength. Background subtraction was conducted using a well in a 96-well plate filled with DI H_2O. Following acquisition, the data was processed with custom code written in Matlab which applied the aforementioned spectral corrections, background subtraction, and was used to fit the data with Lorentzian functions.

Nanotube chirality and DNA sequence-dependent response to LDL

Unsorted DNA-SWCNT samples were diluted to 2 mg/L in PBS and incubated with 0.5 mg/mL LDL (Alfa Aesar) for 18 hours at 37 °C. Chirality-separated samples were diluted to 0.2 mg/L in PBS and incubated with 0.5 mg/mL LDL for 18 hours at 37 °C. Controls were incubated with no LDL present. Photoluminescence spectra were acquired with 2-second exposure times.

Titrations of DNA-nanotube complexes with PEG-conjugated lipids

Unsorted ss$(GT)_6$-DNA-SWCNT samples were diluted to 2 mg/L in PBS and incubated with various concentrations (0-5µM) of two polyethylene glycol (PEG)-conjugated lipids

bioRxiv preprint doi: https://doi.org/10.1101/134999; this version posted May 6, 2017. The copyright holder for this preprint (which was not certified by peer review) is the author/funder. All rights reserved. No reuse allowed without permission.

(Cholesterol-PEG 600, "Cholesterol-PEG", Sigma Aldrich; C16 PEG750 Ceramide, Avanti Lipids). Samples were incubated for 2 hours at 37 °C. Photoluminescence spectra were acquired with 2-second exposure times under 730 nm laser excitation. Polyethylene glycol, with molecular weights of 600 or 750 kDa, diluted in PBS, were used as controls to test for non-specific interactions. To test the effect of lowered pH on sensor performance, samples were diluted in a 100 mM pH 5.5 acetate buffer instead of PBS.

Calculation of normalized Simpson's Index

The Simpson's index is a diversity index used to measure the richness and evenness of a basic data type[50]. The diversity index is maximized when all types of data are equally abundant. When applied to microbiology, the Simpson's Index is referred to as the Hunter-Gaston index[51]. In our application,

$$D = 1 - \frac{1}{N(N-1)} \sum_{j=1}^{S} n_j (n_j - 1)$$

where D is the diversity index, N is the total number of pixels within each cell with detectable nanotube emission, S is the total number of histogram bins, and n_j is the total number of pixels within the jth bin. We obtained the Simpson's Index for each cell, SI_j. For the set of SIj calculated for all the cells in an experiment, we normalized the value obtain the normalized Simpson's Index, nSI.

Cell culture reagents and conditions

RAW 264.7 TIB-71 cells (ATCC, Manassas, VA) were grown under standard incubation conditions at 37˚C and 5% CO_2 in sterile, filtered DMEM with 10% heat-inactivated FBS, 2.5% HEPES, 1% glutamine, and 1% penicillin/streptomycin (all from Gibco). For studies performed with homozygous mutant NPC, compound mutant heterozygote NPC, or wild-type fibroblasts, the respective cell lines, GM18453, GM03123 or GM05659 (Coriell, Camden, NJ) were cultured in MEM with 10% FBS, 2.5% HEPES, and 1% glutamine. Cells were plated on glass bottom petri dishes or lysine-covered glass dishes (MatTek) for fibroblasts. U2OS-SRA cells Chirality-separated SWCNTs were added at 0.2 mg/L in cell culture media (70 µL total volume) and incubated with cells for 30 minutes at 37 °C. This corresponds to approximately 0.5 picogram of SWCNT per cell, for a 50% cell confluency in a 9 mm diameter glass-bottom dish. Cells were imaged immediately, or trypsinized (Gibco), and re-plated on a fresh petri dishes before hyperspectral imaging. All cells were used at 50-70% confluence.

Filipin staining of NPC1 patient-derived fibroblasts

Cells were fixed with 4% paraformaldehyde for 15 minutes, washed 3x with PBS, and stained with Filipin III (Sigma) at a concentration of 50 mg/L for 20 minutes. The cells were then washed 3x with PBS and imaged using a DAPI filter cube.

Cell viability and proliferation assays

RAW 264.7 macrophages were seeded in untreated 96-well plates at 7,000 cells per well. The reporter was introduced to the cells at 0.2 mg/L. Reporter, vehicle (0.027 MSSC + 0.1 M NaSCN), or hydrogen peroxide-treated cells were incubated (times indicated), washed, and detached from the plate with Versene (1x PBS without Mg^{2+}/Ca^{2+}, 5mM EDTA, 2% FBS), pelleted, and incubated with Annexin V Alexa Fluor and Propidium Iodide (Life Technologies). Cells were analyzed by imaging cytometry (Tali) to quantify cell number and fluorophore

bioRxiv preprint doi: https://doi.org/10.1101/134999; this version posted May 6, 2017. The copyright holder for this preprint (which was not certified by peer review) is the author/funder. All rights reserved. No reuse allowed without permission.

content. For proliferation assays, RAW 264.7 macrophages treated with 0.2 mg/L ss$(GT)_6$-(8,6)-SWCNT or vehicle were seeded at 150,000 cells on 100 mm diameter untreated culture dish on day zero. After settling for 10 hours, cells were harvested with Versene (1x PBS without Mg^{2+}/Ca^{2+}, 5mM EDTA, 2% FBS) and by mechanical tapping to remove cells from the surface, stained with Calcein AM, and counted for the initial seeding density. Media was replaced every 2 days. At each 24 hour period, cells were harvested as before and counted. Cell counts represent Calcein AM positive (live) cells.

Lipidomics analyses

Six T-175 flasks were seeded at <50% confluence with RAW 264.7 macrophages in their fifth passage. Three flasks each were treated as follows: control (untreated) or carbon nanotube treated (0.2 mg/mL for 30 minutes, washing, and incubating for 6 hours). Cells were harvested (approx. 80% confluence in each set of flasks) by manual scraping. The flask contents corresponding to each condition were pooled into separate conical tubes and spun to pellet, washed in PBS containing protease inhibitor cocktail (Thermo-Pierce, 88666), pelleted, and flash frozen in a dry ice/IPA slurry with a small head volume of the PBS/inhibitor.

For cell fractionation we adapted a sucrose/iodixanol equilibrium gradient centrifugation procedure for lysosome separation (Thermo, 89839). Briefly, flash frozen cells were thawed and suspended in 2x cpv of PBS/inhibitor, vortexed with reagent included in the kit, and Dounce homogenized with a cooled, tight fitting pestle using 90 strokes (starting cell material was >500mg). After homogenization, reagent was added, tube inverted, and then centrifuged at 4˚C, 500x rcf for 10 minutes. The pellet was stored as the debris/nuclear fraction in all experiments. The supernatant was taken for subsequent ultracentrifugation. Briefly, one day before ultracentrifugation, a sucrose/iodixanol gradient (bottom to top: 30, 27, 23, 20, 17%) was layered into 12 mL polyallomer tubes (Thermo, 03699) and allowed to equilibrate in a cold room inside the metal buckets of an appropriate hanging-bucket rotor. The supernatant from above was mixed with the sucrose/iodixanol gradient to make a final sample density of 15% (total volume, 1 mL), which was then gently layered onto the top of the pre-formed gradient. The buckets were then sealed and moved into the ultracentrifuge using the following settings: ~135,000 rcf (32,000 rpm), 2.5 hours running time, acceleration/deceleration 9/5, 4˚C. The fractionated cell supernatant was removed from the top, and pipetted into six fractions based on volume removed from the ultracentrifuge tube. The volume removed from top to bottom was kept constant across the three conditions. Fractions were frozen until analysis.

Each of the six fractions, plus the nuclear/debris fraction (7 total/condition) was analyzed for the three conditions (21 fractions total). To quantify total protein, a standard curve was produced using BSA mixed into the sucrose/iodixanol gradient (Bradford assay background versus varying gradient was not different). 1x Bradford reagent at room temperature was mixed 1:1 with standard, allowed to incubate in the dark for 30 minutes, and the absorption measured at 595 nm. Each of the fractions was analyzed in this manner after addition of 0.2% IPEGAL CA-630 (non-ionic detergent) to solubilize bound proteins.

Cholesterol quantification was performed (Sigma, MAK043) using a coupled enzyme reaction between cholesterol oxidase and peroxidase with a proprietary colorimetric probe. Cholesterol esterase was used before the reactions to ensure total cholesterol was measured. Briefly, a 3-

bioRxiv preprint doi: https://doi.org/10.1101/134999; this version posted May 6, 2017. The copyright holder for this preprint (which was not certified by peer review) is the author/funder. All rights reserved. No reuse allowed without permission.

phase extraction was performed on each sample fraction (7:11:0.1 chloroform:isopropanol:IPEGAL CA-630). The top aqueous phase and interphase were removed, and the bottom organic phase was vacuum dried. The dried fractions were resuspended in provided buffer and reacted for 1 hour at 37˚C with the supplied reagents and the absorption read at 570 nm. This was compared to a standard curve. Cholesterol levels were normalized by total protein content as measured by the Bradford assay.

Total lipid (total unsaturated hydrocarbon, including cholesterol) was measured after chloroform extracting the samples as above. Briefly, a phospho-vanillin color producing reagent was made by dissolving 5 mg/mL vanillin (Sigma, V1104) in 200 µL neat ethanol, and adding this to the appropriate volume of 17% phosphoric acid. This reagent was stored cool in the dark until needed. Dried sample fractions in glass vials were processed as follows: to each vial was added 200 µL ~98% sulfuric acid. The dried contents were coated with the acid by tipping the vial and vortexing. The vial was placed into a 100˚C mineral oil bath for 20 minutes. The resulting brown/black material was rapidly cooled in wet ice slurry for at least 5 minutes, and 100 µL was placed side-by-side into a 96-well glass plate. To one well, 50 µL of the phospho-vanillin reagent was added, mixed, and the plate incubated in the dark for 12 minutes. Absorption of each well (reagent reacted and sulfuric acid background) was taken at 535 nm. The difference was the measurement, which was compared to a standard curve that used Oleic acid (Sigma, O1008), prepared using the above protocol, as a model unsaturated hydrocarbon material. Total lipid levels were normalized by total protein content.

Extraction and differentiation of bone marrow-derived macrophages

Bone marrow derived cells (BMDM) were prepared from 6 week-old C57/Bl6 mice and cultured in the presence of 10 ng/ml of recombinant CSF-1[46]. Cells were collected 3, 5 and 7 days post-isolation and submitted to flow cytometry analysis for expression of the differentiation markers Gr-1 (monocytes/granulocytes-1/200), Cd11b (macrophages-1/200), F4/80 (mature macrophages-1/50). Cells were incubated with 1 µl of Fc Block (BD Biosciences) for every million cells for at least 15 minutes at 4°C. Cells were then stained with the appropriate antibodies (BD Biosciences) for 20 minutes at 4°C, washed with FACS buffer, and resuspended in FACS buffer containing DAPI (5 mg/ml diluted 1:5,000) for live/dead cell exclusion[47].

LysoTracker-nanotube colocalization

RAW 264.7 or BMDM macrophages were incubated with Cy5-ss$(GT)_6$-HiPco nanotubes for 30 minutes at a concentration 1 mg/L. The cells were then washed 3x with PBS and placed in fresh cell media. Six hours later, the cells were incubated with 5 nM LysoTracker Green DND-26 (Life Technologies) for 15 minutes in cell media, washed 3x with PBS, and imaged immediately in fresh PBS. The FITC or Cy5 channels were used for LysoTracker Green or Cy5-ss$(GT)_6$-HiPco nanotubes, respectively. Plates of cells containing only Cy5-ss$(GT)_6$-HiPco nanotubes or LysoTracker Green were used as controls to test for bleed-through across channels.

Atomic force microscopy (AFM)

A stock solution of ss$(GT)_6$-(8,6)-SWCNTs at 7 mg/L in 100 mM NaCl was diluted 20x in dH_2O and plated on a freshly cleaved mica substrate (SPI) for 4 minutes before washing with 10 mL of dH_2O and blowing dry with argon gas. An Olympus AC240TS AFM probe (Asylum Research)

bioRxiv preprint doi: https://doi.org/10.1101/134999; this version posted May 6, 2017. The copyright holder for this preprint (which was not certified by peer review) is the author/funder. All rights reserved. No reuse allowed without permission.

in an Asylum Research MFP-3D-Bio instrument was used to image in AC mode. Data was captured at 2.93 nm/pixel XY resolution and 15.63 pm Z resolution.

Statistics

Statistical analysis was performed with GraphPad Prism version 6.02. All data met the assumptions of the statistical tests performed (i.e. normality, equal variances, etc.). Experimental variance was found to be similar between groups using the F-test and Brown-Forsythe test for unpaired t-tests and one way ANOVAs, respectively. To account for the testing of multiple hypotheses, one way ANOVAs were performed with Dunnet's, Tukey's, or Sidak's post tests when appropriate. Sample size decisions were based on the instrumental signal-to-noise ratios.

Cell line source and authentication

RAW 264.7 and U2OS cells were acquired from ATCC, and were tested for mycoplasma contamination by the source. Primary bone-marrow derived monocytes were tested for mycoplasma contamination using Dapi staining. Patient-derived fibroblasts were obtained from Coriell and tested for mycoplasma contamination by the source.

Code availability

Matlab code for the data analysis in this manuscript is available upon request, by contacting the corresponding author (hellerd@mskcc.org).

bioRxiv preprint doi: https://doi.org/10.1101/134999; this version posted May 6, 2017. The copyright holder for this preprint (which was not certified by peer review) is the author/funder. All rights reserved. No reuse allowed without permission.

Figures:

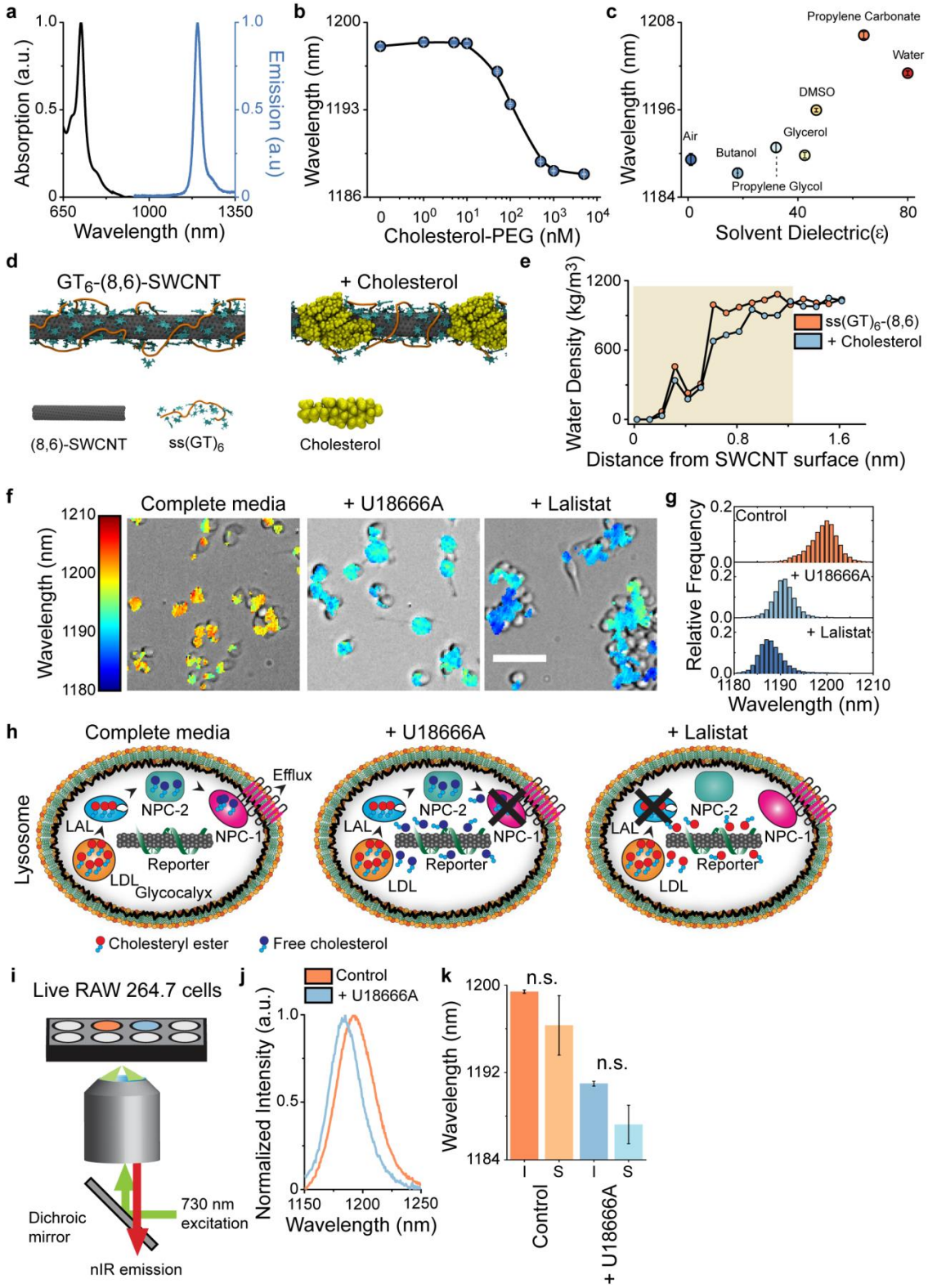

bioRxiv preprint doi: https://doi.org/10.1101/134999; this version posted May 6, 2017. The copyright holder for this preprint (which was not certified by peer review) is the author/funder. All rights reserved. No reuse allowed without permission.

Figure 1. Optical response of carbon nanotube complexes to lipid environments. a, Normalized absorption and emission spectra of ss$(GT)_6$-carbon nanotube complexes purified to isolate the (8,6) species. **b,** Emission peak wavelength of ss$(GT)_6$-(8,6) nanotube complexes in solution as a function of cholesterol-PEG concentration. Error bars are standard error of the mean, obtained from 3 technical replicates performed for each concentration. **c,** Mean emission wavelength of ss$(GT)_6$-(8,6) nanotube complexes exposed to different solvents. Error bars are standard errors of the mean, obtained from 5 technical replicates for each solvent. **d,** Frames from all-atom molecular dynamics simulations of equilibrated structures of the ss$(GT)_6$-(8,6) nanotube complex in water, and the same complex equilibrated in the presence of cholesterol. **e,** Water molecule density as a function of distance from the center of the equilibrated ss$(GT)_6$-(8,6) nanotube complex and the same complex equilibrated in the presence of cholesterol. **f,** Overlay of transmitted light with hyperspectral image of RAW 264.7 macrophages incubated with ss$(GT)_6$-(8,6) complex under the specified treatments. Color legend maps to nanotube emission peak wavelength. Scale bar = 50 µm. **g,** Histogram of emission wavelengths of all pixels from the hyperspectral images, bin size of 1 nm. **h,** Proposed schematics of the proposed function of the ss$(GT)_6$-(8,6) nanotube complexes in macrophages treated with U18666A or Lalistat. **i,** Schematic of the optical setup for high-throughput measurements of ss$(GT)_6$-(8,6) emission in live cells. **j,** Spectra of ss$(GT)_6$-(8,6) emission from live RAW 264.7 cells incubated in normal media (control), and in media with U18666A. **k,** Mean center wavelengths of ss$(GT)_6$-(8,6) emission from n = 5 technical replicates, acquired using hyperspectral imaging (I) and spectroscopy (S). Mean values were compared using a one way ANOVA with Tukey's multiple comparison test. Error bars are standard error of the mean.

bioRxiv preprint doi: https://doi.org/10.1101/134999; this version posted May 6, 2017. The copyright holder for this preprint (which was not certified by peer review) is the author/funder. All rights reserved. No reuse allowed without permission.

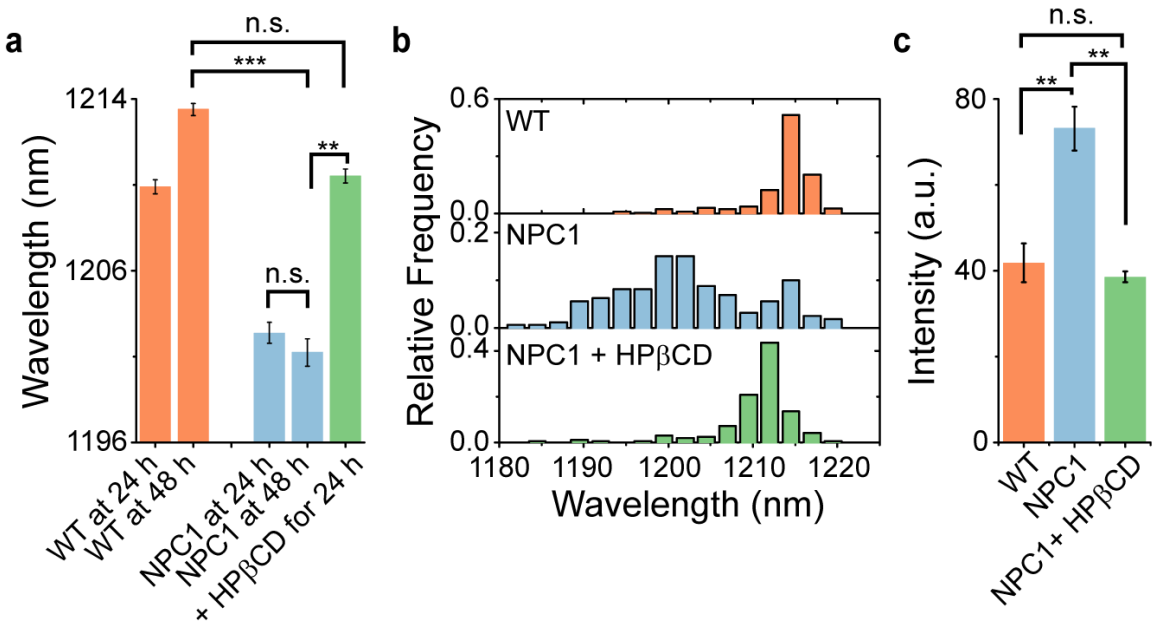

Figure 2. Measurement of lipid accumulation in NPC1 patient-derived fibroblasts. a, Mean reporter emission from wild-type fibroblasts, patient-derived NPC1 fibroblasts, and NPC1 fibroblasts treated with hydroxypropyl-β-cyclodextrin (HPβCD) for 24 hours. Statistical significance was determined with a one-way ANOVA with Sidak's multiple comparison test. **b,** Histograms of the nanotube emission wavelength from single LE/Ly of wild-type fibroblasts, NPC1 patient fibroblasts, and NPC1 fibroblasts treated with HPβCD for 24 hours. **c,** Mean filipin intensity from WT fibroblasts, NPC1 cells, and NPC1 cells treated with HPβCD for 24 hours, at 48 hours after nanotube addition. Statistical significance was determined with a one-way ANOVA with Tukey's multiple comparison test. All error bars are S.E.M. from 3 technical replicate experiments. * = $p<0.05$, ** = $p<0.01$, *** = $p<0.001$.

bioRxiv preprint doi: https://doi.org/10.1101/134999; this version posted May 6, 2017. The copyright holder for this preprint (which was not certified by peer review) is the author/funder. All rights reserved. No reuse allowed without permission.

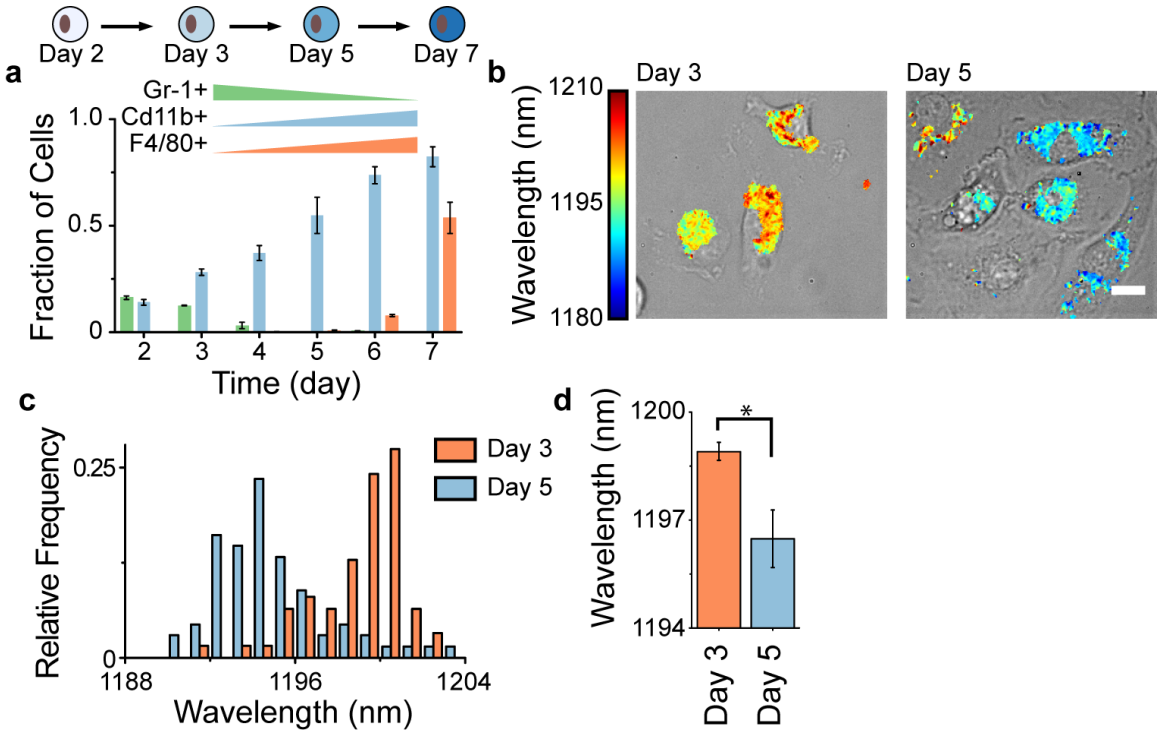

Figure 3. Changes in the lysosomal lipid content in maturing bone marrow-derived monocytes. a, Temporal changes in expression of the macrophage markers Cd11b and F4/80 and monocyte/granulocyte marker Gr-1 in murine bone marrow-derived cells in the presence of CSF-1. Error bars denote standard deviations from n = 8 mice. **b,** Overlaid brightfield and hyperspectral images of the reporter in maturing bone marrow-derived cells at days 3 and 5 after harvesting. **c,** Histogram of the mean reporter emission, measured per cell, at days 3 and 5 after harvesting. **d,** Differences in the mean reporter emission from cells at days 3 and 5, from n = 4 mice. Values were compared using an unpaired t-test, $p < 0.05$. Scale bars = 10 µm.

bioRxiv preprint doi: https://doi.org/10.1101/134999; this version posted May 6, 2017. The copyright holder for this preprint (which was not certified by peer review) is the author/funder. All rights reserved. No reuse allowed without permission.

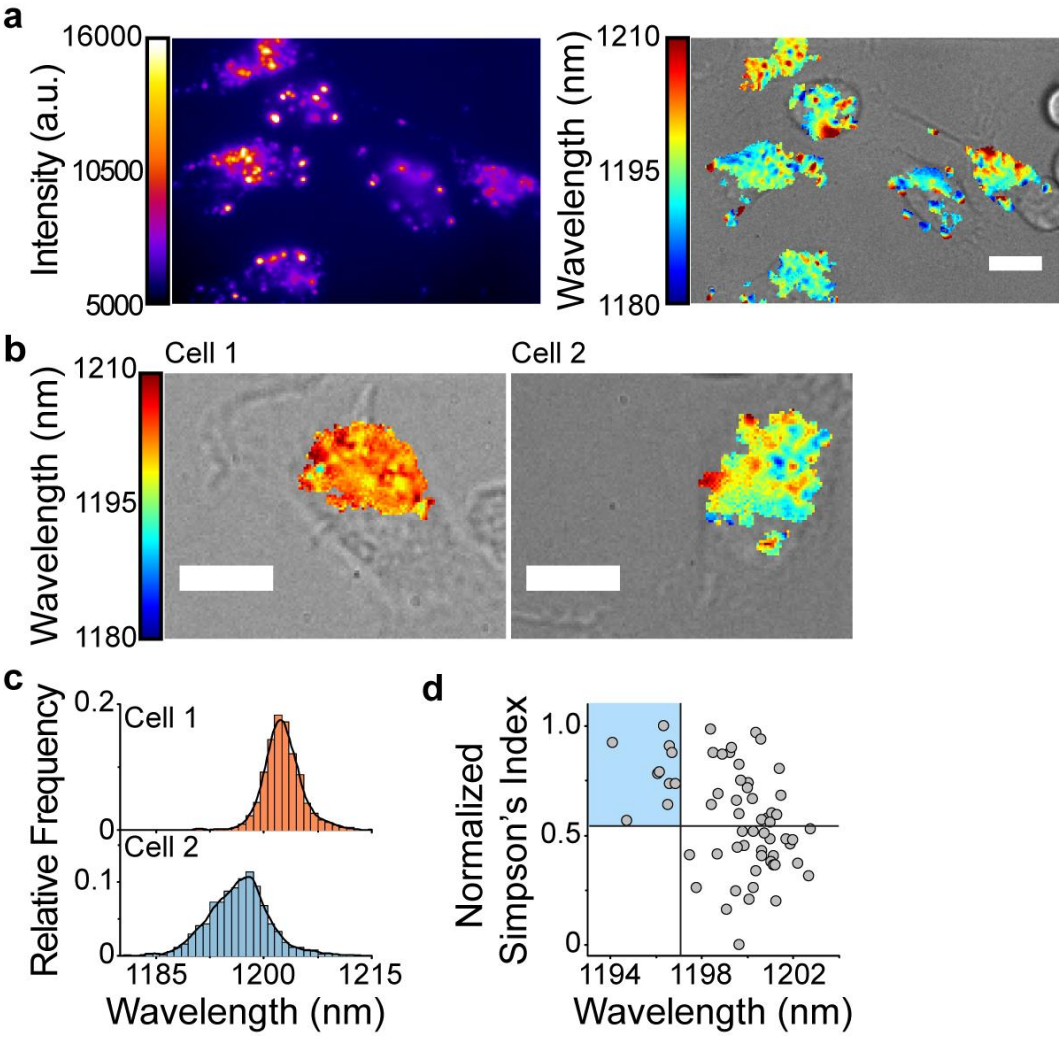

Figure 4. Quantifying intracellular heterogeneity in monocyte lysosomes. a, Near-infrared broadband and overlaid brightfield/hyperspectral images of the reporter in bone marrow-derived cells after 3 days of CSF-1 treatment. **b,** Endolysosomal lipid maps of the reporter in bone marrow-derived cells at day 3 of maturation. **c,** Corresponding histogram of reporter emission from emissive pixels within the two cells. Bin size = 1 nm. **d**, Scatterplot of the normalized Simpson's Index against the mean emission wavelength per cell for n = 64 cells. Scale bars = 10 µm.

bioRxiv preprint doi: https://doi.org/10.1101/134999; this version posted May 6, 2017. The copyright holder for this preprint (which was not certified by peer review) is the author/funder. All rights reserved. No reuse allowed without permission.

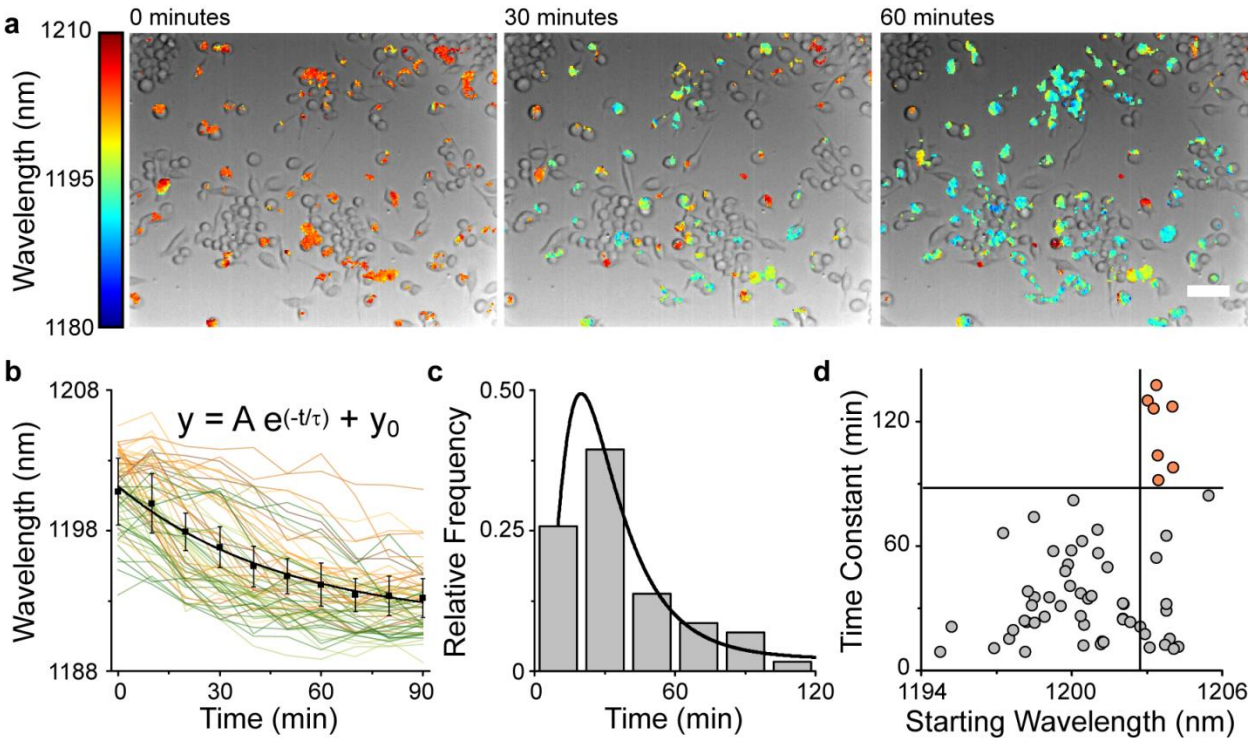

Figure 5. Single-cell kinetics of lipid accumulation. a, Overlaid brightfield and hyperspectral images of the reporter emission in RAW 264.7 macrophages upon addition of acLDL (100 µg/mL) and U18666A (3 µg/mL) to LPDS media at t = 0, 30 minutes, and 60 minutes. Scale bar = 50 µm. **b,** Single-cell trajectories of lysosomal lipid accumulation from 60 cells. Black curve is the mean. Error bars are standard deviation from n = 4 technical replicates. **c,** Distribution of time constants of lipid accumulation in single cells fitted to a log-normal distribution. Bin size = 20 nm. **d,** Scatter plot of the time constants vs. starting emission wavelength, n = 60 cells.

bioRxiv preprint doi: https://doi.org/10.1101/134999; this version posted May 6, 2017. The copyright holder for this preprint (which was not certified by peer review) is the author/funder. All rights reserved. No reuse allowed without permission.

Acknowledgements

This work was supported by the NIH Director's New Innovator Award (DP2-HD075698), NIH grants R37-DK27083, R01CA148967, R01CA181355, and P30 CA008748 cancer center support grant, the Anna Fuller Fund, the Louis V. Gerstner Jr. Young Investigator's Fund, the Experimental Therapeutics Center, Mr. William H. Goodwin, Mrs. Alice Goodwin, the Commonwealth Foundation for Cancer Research, the Honorable Tina Brozman Foundation, the Alan and Sandra Gerry Metastasis Research Initiative, Cycle for Survival, the Frank A. Howard Scholars Program, and the Center for Molecular Imaging and Nanotechnology at Memorial Sloan Kettering Cancer Center. P.V.J. was supported by an NIH NCI-T32 fellowship (2T32CA062948-21). D.R. was supported by an American Cancer Society 2013 Roaring Fork Valley Research Fellowship. C.P.H. was supported by an NIH NCI-T32 (CA062948) fellowship. J.M. was supported by the U.S. Department of Energy (DOE), Office of Science, Basic Energy Sciences (BES) under Award DE-SC0013979. T.V.G. was supposed by the Frank Lappin Horsfall, Jr. Fellowship. L.A. was supported by the American Brain Tumor Association. J.B. was supported by a Tow Fellowship Award from the Center for Molecular Imaging and Nanotechnology, Memorial Sloan Kettering Cancer Center. We thank the Molecular Cytology Core Facility at Memorial Sloan Kettering Cancer Center and the Electron Microscopy & Histology Core Facility at Weill Cornell Medical College. Use of the high-performance computing capabilities of the Extreme Science and Engineering Discovery Environment (XSEDE), supported by the National Science Foundation (NSF) grant numbers TG-MCB-120014 and TG-MCB-130013, is gratefully acknowledged. We also thank Y. Shamay, A. Erez, R. Williams, R. Langenbacher, and J. Shah for helpful discussions, and J. Bartlett for aid in manuscript preparation.

bioRxiv preprint doi: https://doi.org/10.1101/134999; this version posted May 6, 2017. The copyright holder for this preprint (which was not certified by peer review) is the author/funder. All rights reserved. No reuse allowed without permission.

Author Contributions

All authors participated in designing the experiments, discussing the results, and helping to edit the manuscript. P.V.J., D.R., T.V.G. and D.A.H. conceived and developed the technology and co-wrote the manuscript. P.V.J, D.R., T.V.G, C.H., D.B.I, J.B., and J.H. performed experiments and analysis. L.A. performed the FACS work and extracted BMDM from mice. N.H.P. and A.S.H. assisted with the macrophage experiments.

Supplementary information

Supplementary Text

Supplementary Figures 1-36

Supplementary Video 1-3

Supplementary Table 1

Competing financial interests

The authors declare no competing financial interests.